The International Journal of Advanced Manufacturing Technology
https://doi.org/10.1007/s00170-025-17075-5

ORIGINAL ARTICLE

Manufacturability and microstructure of AlSi10Mg/SiC composites with different volume fractions of SiC using laser powder bed fusion

Achim Conzelmann[1,2] · **Hans Jürgen Seifert**[2] · **Hadi Mozaffari-Jovein**[1,3]

Received: 8 July 2025 / Accepted: 18 November 2025
© The Author(s) 2025

Abstract

In the present study commercially available AlSi10Mg and SiC powders were mixed in a tumble mixer with resulting compositions of 5, 15 and 25 vol% SiC and processed using laser powder bed fusion. Different process parameters were used to manufacture samples which were characterized by various properties, such as porosity, microstructure and occurring phases to evaluate the manufacturability of the powder mixtures. The samples showed increasing porosity with lowered volumetric energy density and increasing SiC content. Relative densities of about 93.0% (25 vol% SiC), 94.5% (15 vol% SiC) and 98.5% (5 vol% SiC) respectively could be achieved. In addition, the correlation between the used energy density and the retained SiC particles in the samples was investigated. The quantity of retained SiC particles correlates negatively with the achievable density for all compositions, making compromises between these two properties necessary depending on the desired application. It is shown that SiC can get dissolved due to the high absorption of the laser energy resulting in the formation of primary silicon crystals as well as Al_4C_3 and Al_4SiC_4 phases. Microstructure characterizations using AFM revealed the influence of the SiC fraction on the eutectic structure and the formation of the new phases. Finally, EDS and TOF-SIMS analysis showed that the formed Al_4C_3 phase can react with the humidity of ambient air at the surface, leading to localized cracks due to AlOOH formation.

Keywords Additive manufacturing · Laser powder bed fusion · AlSi10Mg/SiC composites · Metal matrix composite · Microstructure

1 Introduction

Laser powder bed fusion (LPBF) is an additive manufacturing (AM) process which uses a laser to fuse metallic powders layer by layer to form three-dimensional parts according to input CAD data [1–3]. The LPBF process offers several advantages over traditional manufacturing methods, including the ability to produce parts with complex geometries, lower lead times, reduced materials waste and minimal or no tooling requirement [2–4]. Additionally, rapid solidification (10^3–10^8 K/s) occurs in the small melt pools, resulting in refined grains and improved mechanical properties of parts [5, 6]. Because of these aspects LPBF has a wide range of applications in various industries, such as aerospace, automotive and medical [7–10]. In the aerospace industry LPBF is used to produce parts like engine blades [7], in the automotive industry to manufacture lightweight structural parts such as wishbones or brake calipers [8] and in the medical industry to fabricate implants, including hip and knee replacements, with customized geometries and improved fit [9, 10]. Increasing usage of LPBF opens it up for new fields of application like metal-matrix-composites (MMCs). MMCs are generally used to improve the mechanical properties or the wear resistance of the used alloy [11], but can also be used to functionalize the material, e.g. to create abrasive properties for grinding applications [12]. Adding reinforcements like SiC, TiC, TiB_2, Al_2O_3 and others to aluminum alloys has been investigated for years [13–16].

✉ Achim Conzelmann
achim.conzelmann@hs-furtwangen.de

1 Institute of Materials Science and Engineering Tuttlingen (IWAT), Furtwangen University, Kronenstraße 16, Tuttlingen 78532, Germany

2 Institute for Applied Materials (IAM-AWP), Karlsruhe Institute of Technology (KIT), Kaiserstraße 12, Karlsruhe 76131, Germany

3 Department of Microsystems Engineering, University of Freiburg, Georges-Köhler-Allee 103, Freiburg 79110, Germany

Published online: 29 December 2025

Particularly, SiC has been a focus in research, due to its high hardness, modulus, excellent thermal conductivity, strong wear resistance and low cost [17]. Aluminum/SiC MMCs combine the ductility and specific strength of the Al matrix with the high modulus and hardness of the SiC resulting in outstanding properties [14, 17]. As a result, they have been successfully integrated in aerospace and automotive fields [17]. However, traditional manufacturing, such as casting or powder metallurgy, limits the possible geometrical shapes and functionality of the products, which would be significantly improved using AM [18]. For this reason, the additive manufacturing of SiC particle reinforced aluminum matrix composites has attracted some interest in the last few years.

Various manufacturing processes such as additive manufacturing using cold gas spraying [19] or direct energy deposition (DED) [20] have been investigated, with most research focusing on laser powder bed fusion. While Astfalck et al. [21] investigated AlSi12 as a potential matrix material, most research has been done using the AlSi10Mg alloy as matrix [22–25]. It is reported, that with the addition of SiC particles, the absorptivity of the used powder increases due to the high absorptivity of SiC (78% [26]) compared to aluminum (25% [27]) [25]. The addition of SiC particles also changes the resulting properties. Wang et al. [28] discovered an increase of the tensile strength and hardness when preparing 2 vol% SiC/AlSi10Mg nano composites compared to the pure alloy. Chang et al. [23] analyzed the influence of varying SiC particle diameters and found that as the SiC diameter decreased, the in-situ reaction increased, resulting in higher microhardness and improved wear resistance. A similar trend was observed in the research by Xue et al. [29]. Despite the high cooling rates and resulting short interaction times, chemical reactions between the aluminum matrix and the SiC particles have been observed. Some studies report the formation of Al_4C_3 [21, 24], an undesirable phase due to its instability in moist environments, whereas others identify the more stable Al_4SiC_4 phase as the reaction product [22, 23, 29]. Table 1 shows the process parameters specified in these studies. These differ drastically, even when comparing the volumetric energy density (VED) making comparisons almost impossible. VED is a common value to compare experiments while using different equipment and machines [1, 6]. It is a calculation of the energy supplied by the laser beam to a volumetric unit of powder and therefore a key factor that affects the density of parts fabricated by LPBF. To calculate VED the laser power $P\ (W)$, scan speed $v\ (mm/s)$, hatch spacing $h\ (mm)$ and layer thickness $s\ (mm)$ are used as shown in Eq. 1.

$$VED = \frac{P}{v \bullet h \bullet s} \tag{1}$$

While, as mentioned above, some studies have been conducted on additive manufacturing of AlSi10Mg/SiC composites, there still remain questions to be answered. The formation mechanisms of Al_4SiC_4 respective Al_4C_3 phases are of particular interest, as Al_4C_3 formation is undesirable due to its reactivity with water and moist environments. Additionally, most studies focus on the manufacturing of dense samples and neglect the breakdown of SiC. The aim of this study is therefore to gain a better understanding of the influence different LPBF process parameters have on the manufacturability and microstructure of AlSi10Mg/SiC samples while trying to keep the SiC fraction constant during the process. In order to analyse the influence of the SiC particles, different volume fractions of 0, 15 and 25 vol% respectively are investigated.

2 Experimental procedures

2.1 Materials and sample preparation

Commercially available, mostly spherical shaped AlSi10Mg alloy powder particles (Concept Laser GmbH, Lichtenfels) with a chemical composition according to Table 2 and irregular shaped α-SiC particles (Washington Mills Inc., North Grafton) with a maximum free carbon content of 0.3% according to the manufacturer's specifications were used as starting powders and are shown in Fig. 1a) and c).

Table 1 Reported LPBF process parameters for different Al/SiC composites

SiC	*P* (W)	v (mm/s)	h (µm)	s (µm)	VED (J/mm^3)	Relative Density (%)	
8.5 vol%	350	2500	50	50	56	-	[30]
10 vol%	200	375	150	50	71	97.4	[21]
15 wt%	500	1200	120	40	87	97.8–98.9	[29]
15 wt%	490	900	120	40	113	97.7	[31]
5 vol%	195	880	50	30	148	-	[24]
10 vol%	195	640	50	30	203	-	
20 wt%	100	100	50	50	400	96	[22]
20 wt%	100	100	50	30	666	85–97	[23]

Table 2 Chemical composition of the used AlSi10Mg powder according to the provided material certificate

Element	Si	Mg	Mn	Fe	Ni	Zn	Pb	Sn	Al
wt%	9.6	0.38	0.003	0.12	0.005	<0.005	<0.02	<0.01	Balance

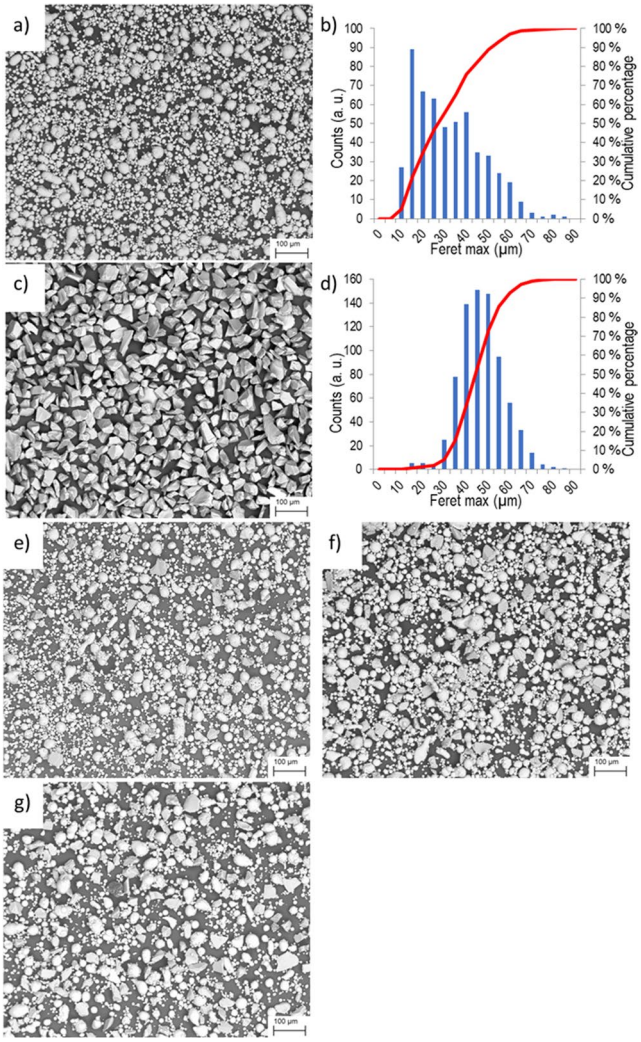

Fig. 1 SEM images (250x) of the starting powders (**a**) AlSi10Mg with (**b**) particle size distribution of AlSi10Mg and (**c**) SiC with (**d**) particle size distribution of SiC, as well as the powder mixtures (**e**) 5 vol% SiC/AlSi10Mg, (**f**) 15 vol% SiC/AlSi10Mg and (**g**) 25 vol% SiC/AlSi10Mg

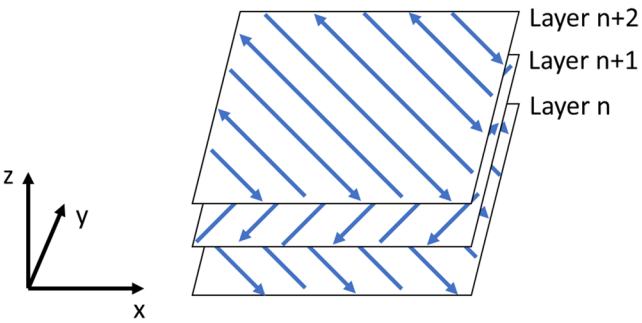

Fig. 2 Schematic display of the used scanning strategy

Table 3 Process parameters used for the first parameter screening

Level	*P* (W)	v (mm/s)	h (mm)	s (mm)
−2	90	200	0.050	0.025
−1	92	300	0.075	0.025
0	95	450	0.100	0.025
1	98	600	0.125	0.025
2	100	700	0.150	0.025

Particle sizes of both powders were chosen in a similar range with values of 10 µm to 63 µm (D_{50}=29 µm) for the AlSi10Mg and 15 µm to 63 µm (D_{50}=45 µm) for the SiC powder respectively. Particle sizes were provided by the vendor and confirmed experimentally using the shadow projection technique with an optical microscope in combination with ImageJ. The size distributions of the powders are shown in Fig. 1b) and d). Both powders were mixed in a lab sized tumble mixer with compositions of 5, 15 and 25 vol% SiC respectively. The mixing process was performed with 20 rpm for 2 h allowing the SiC powder to disperse homogeneously while maintaining its shape, as shown in Fig. 1e) to g).

2.2 LPBF processing of the powder mixtures

To manufacture the samples a Concept Laser Mlab Cusing 100R laser powder bed fusion system was used. The machine utilizes a Yb-Fibre laser with 1030 nm wavelength and laser power up to 100 W. An argon atmosphere was used with a maximum oxygen-content of <0.5% dropping below 0.1% during the first 10 layers of manufactured support structure. All specimens were built using a layer thickness of 25 µm with a standard x/y raster strategy. Between consecutive layers the direction of scanning was rotated by 90°, as shown in Fig. 2. Cubic samples with 5 mm x 5 mm x 5 mm were manufactured on 2 mm of support structure which served as an oxygen getter and to improve part removal. A sandblasted 90 mm x 90 mm build plate made of 6061 aluminum alloy was used as substrate.

To start the experiments a parameter screening was done for the powder mixture containing 25 vol% SiC using a central composition DoE based on parameters for the *pure* AlSi10Mg alloy, since literature values for different composites vary drastically, as shown in Table 1. The used process parameters are shown in Table 3. Subsequently parameters were optimized for all powder compositions varying scan speed and hatch spacing while keeping the laser power constant at 92 W. Optimized parameters were then used for the following analytical steps and are shown in Sect. 3.1 of

this publication. At least two samples were prepared for all parameters in order to check reproducibility.

2.3 Analysis of the manufactured samples

The samples from the first parameter screening were evaluated by optical inspection to exclude parameters which resulted in severe deformations, discolorations or other visible defects. Additionally, densities (ρ) were measured in ethanol using Archimedes Principle. Measurements were repeated at least 5 times per specimen. All 10 measurements for one process parameter set were used to calculate the average and standard deviation. The theoretical density of the composite samples

ρ_{TD} was calculated using Eq. (2), where ρ_{SiC} and $\rho_{AlSi10Mg}$ are the densities of SiC (3.21 g/cm³) and AlSi10Mg (2.68 g/cm³), respectively, while V_{SiC} and $V_{AlSi10Mg}$ refer to their corresponding volume fractions.

$$\rho_{TD} = \rho_{SiC} \bullet V_{SiC} + \rho_{AlSi10Mg} \bullet V_{AlSi10Mg} \quad (2)$$

The resulting relative density ρ_{RD} was defined as follows (Eq. 3) where ρ is the average of the measurements.

$$\rho_{RD} = \frac{\rho}{\rho_{TD}} \bullet 100\,\% \quad (3)$$

Computer tomographic (CT) scans using a GE phoenix v|tome|x s240 were performed on selected samples to validate the measurements as well as further evaluate the distribution of pores and cracks. CT scans were assessed using the software VGStudio MAX by Volume Graphics. Phases were analyzed using a Bruker D8 Discover with Cu Kα radiation at 40 kV and 40 mA between 20° and 90° two-theta. In order to observe the microstructure of the specimens they were ground from grit 320 to 2000 and subsequently polished with 3 µm to 1 µm diamond suspension and 0.1 µm Eposil F from QATM. Unetched samples were examined using an atomic force microscope (AFM, Park Systems NX10) and an optical microscope (Zeiss AX10). The SiC content of the manufactured samples was determined with the software ImageJ. At least three different regions per sample were examined at 200x magnification and the average and standard deviation of all measurements were calculated. Furthermore, polished specimens were left in ambient atmosphere for a prolonged period of time to provoke surface reactions and subsequently observed using a scanning electron microscope (FIB-SEM, Zeiss Crossbeam 550) equipped with an energy-dispersive spectrometer (EDS, Oxford Instruments ULTIM MAX). Additionally, time-of-flight secondary ion mass spectroscopy (TOF-SIMS, TOFWERK fibTOF) was used in combination with the FIB-SEM to evaluate depth profiles. During FIB milling, the material is removed by mechanical atomization and ionization. The milling process is performed in raster mode and also provides the source for secondary ion mass spectroscopy. The material is sputtered away frame by frame and the secondary ions (SI) are generated from an increasing depth of the sample. The secondary ions are extracted and passed through the TOF-SIMS analyzer, generating mass spectra for each point on the map.

3 Results

3.1 Screening run (25 vol. SiC/AlSi10Mg) and subsequent optimization

In the first parameter study for the powder mixture containing 25 vol% SiC the VED was varied between 49 and 190 J/mm³ and its results are shown in Table 4. The overall experimental design comprised 20 experimental points, including 6 center replicate points based on the parameters of pure AlSi10Mg alloy. In addition to the relative densities, the optical appearance was evaluated and classified. Sample no. 13 had to be aborted during the building process due to excessive warping. It is shown that the relative density plateaus at around 93% with VEDs above 75 J/mm³ while below that value the density drops to 87%.

Evaluating the optical appearance of the manufactured cubes is especially interesting when comparing high and low VEDs. While samples with low to medium energy density up to 100 J/mm³ don't show any significant anomaly in appearance, specimen manufactured with higher energy density display a deformation of the top surface for all samples. Figure 3 shows the top view of the build plate (a) after the LPBF process in combination with CT scans (b) from sample no. 7 (low VED) and sample no. 11 (high VED) visualizing the severe deformation of the surface of sample no. 11. The CT scans additionally show vastly different pore structures with far more pores in the sample which was manufactured using lower energy density, confirming the measurements done by Archimedes Principle. In contrast more cracks, especially near the edges, were detectable in the specimen produced at higher energy density.

Exemplary microstructures in xy-direction of the specimens produced during the screening experiments with 25 vol% SiC are shown in Fig. 4. With lower energy density used, higher porosity can be observed, supporting the density measurements. The hatching distances used are directly visible in all samples and are marked in the micrographs. A chessboard-like pattern, in which the SiC particles appear concentrated, can be clearly recognized between the scanned laser tracks. The amount of observable SiC particles

Table 4 Parameters, relative densities and optical classification (bad = surface deformation, good = no surface deformation) of the 25 vol% SiC screening run

Sample no.	*P* (W)	v (mm/s)	h (mm)	VED (J/mm^3)	Relative Density (%)	Optical Classification
1	92	300	0.075	163.56	92.86	Bad
2	98	300	0.075	174.22	92.97	Bad
3	92	600	0.075	81.78	90.33	Good
4	98	600	0.075	87.11	90.89	Good
5	92	300	0.125	98.13	92.22	Good
6	98	300	0.125	104.53	92.56	Bad
7	92	600	0.125	49.07	87.19	Good
8	98	600	0.125	52.27	87.58	Good
9	90	450	0.100	80.00	92.77	Good
10	100	450	0.100	88.89	93.33	Good
11	95	200	0.100	190.00	93.53	Bad
12	95	700	0.100	54.29	87.25	Good
13	95	450	0.050	168.89	-	-
14	95	450	0.150	56.30	88.06	Good
15	95	450	0.100	84.44	92.94	Good
16	95	450	0.100	84.44	93.10	Good
17	95	450	0.100	84.44	93.23	Good
18	95	450	0.100	84.44	93.01	Good
19	95	450	0.100	84.44	93.21	Good
20	95	450	0.100	84.44	93.23	Good

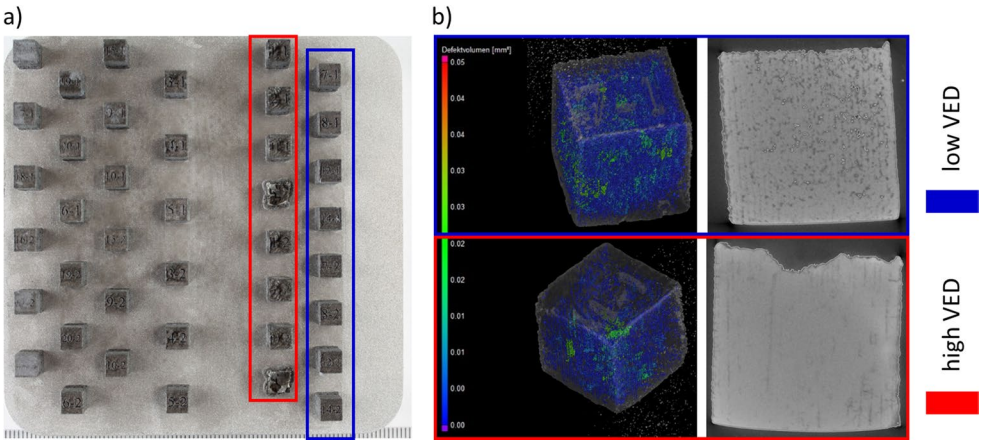

Fig. 3 Visualization of the samples (5 mm x 5 mm x 5 mm) produced in the screening run. (**a**) 90 mm x 90 mm build plate with high (> 150 J/mm^3, red) and low (< 60 J/mm^3, blue) VEDs marked; (**b**) 3D CT scans with visualized pores (left) and 2D sections (right) for samples no. 7 (top) and no. 11 (bottom)

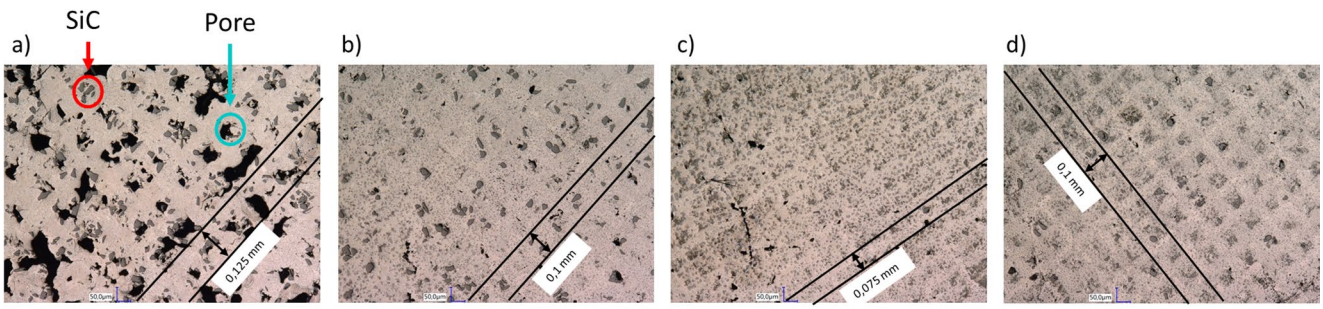

Fig. 4 Light microscopic images (300x) for samples with 25 vol% SiC, manufactured using (**a**) 49 J/mm^3, (**b**) 84 J/mm^3, (**c**) 163 J/mm^3, (**d**) 190 J/mm^3 with marked hatch spacings

decreases significantly with higher VED and smaller hatch spacing.

Based on these results, further parameter optimizations were done with the goal to compromise between low porosity and retaining most of the SiC particles in the produced samples. For these, the laser power was kept constant at 92 W and the layer thickness at 0,025 mm while the scanning speed and the hatch spacing were varied. Subsequently, parameters for 15 vol% and 5 vol% SiC were developed using the same methodology. Resulting densities as well as the amount of retained SiC are shown in Fig. 5 for the different compositions. Comparing the graphs makes it clear that a lower SiC content of only 5 vol% increases the possible density to nearly 98.5%. Additionally, Fig. 5 shows that higher VEDs corelate with a significant reduction of SiC particles in the samples for all compositions.

For further analysis one process parameter set for each of the respective powder mixtures was chosen. These are shown in Table 5. Detailed results for samples manufactured using these parameters are presented in the following sections.

3.2 Phase characterization using x-ray diffraction

Figure 6 shows the XRD diffractograms of the starting powder compositions compared to the respective LPBF fabricated composite samples. While the phases present in the powder diffractograms are α-Al, Si and SiC, additional reflexes can be observed in the processed samples. These can be identified as the carbides Al_4C_3 or Al_4SiC_4. When comparing the diffractograms of the starting powders with the fabricated samples, it is evident, that the intensity of the silicon reflexes increases substantially, especially for the samples with 15 and 25 vol% SiC.

3.3 Effects of SiC additions on microstructural evolution

To compare the influence of different SiC fractions, a combination of LM and AFM images is shown in Fig. 7 highlighting the differences in density, particle distribution and microstructure. AFM measurements were performed both far away and in close proximity to SiC particles to evaluate their influence on the microstructure. Samples with 5 vol% SiC show a typical melt pool structure observed in LPBF fabricated AlSi10Mg alloys which is visible in areas with and without SiC particles. The melt pool structure is composed of a eutectic network with small cell sizes in the middle of the melt pools (MP fine), larger cell size at the edge of the melt pools (MP coarse) and a heat affected zone surrounding the melt pools (HAZ), as exemplarily indicated in the AFM image. In addition, a new plate-like phase, most likely Al_4C_3 or Al_4SiC_4, is visible in direct proximity to the SiC particles while none of it is visible in areas far from SiC particles. This changes in the sample with 15 vol% SiC starting composition where the new phase can be observed in the whole sample. While the typical eutectic network described above is still visible in areas away from the SiC particles, its morphology changes in the vicinity of the SiC particles, where the silicon is concentrated in larger clusters and the network becomes incoherent. Additionally, primary silicon crystals become evident, especially near SiC particles. These increase significantly in size when analyzing the sample with an initial composition of 25 vol% SiC. In this sample the eutectic network changed its morphology throughout the whole sample and substantially more of the plate-like phase is visible. In all samples the SiC particles show good bonding with the matrix with no cracks or pores at the interface. The morphology of the particles remains mostly sharp-edged, although some rounding can be observed in the sample with 5 vol% SiC.

SEM images as well as the corresponding results from EDS measurements at different positions in a polished sample with 15 vol% SiC, which was exposed to ambient air over a prolonged period of time in order to induce surface reactions, are shown in Fig. 8. Again, no cracks or micropores are observable in the interface between SiC and matrix. Of particular interest is the measurement of occurring oxygen. Figure 8a) shows that there is a distinct zone in the immediate vicinity of the SiC particle in which there is no noticeable increase in oxygen concentration while the carbon concentration in combination with the SEM image clearly indicates lamellar carbide formation. In the same area an increased Si concentration can be observed in some spots. All described zones fit to the observed contrast changes in the Al map. With increasing distance from the SiC particle, an increase in the oxygen concentration can be observed, which correlates with the presence of carbon and a visual change of the plate-like phase in the SEM image from a very light grey to a dark grey. Figure 8b) shows one of the oxygen rich areas in detail confirming the observations made before. Additionally, cracks in the plate-like phase become visible.

To further analyze the occurring oxygen, TOF-SIMS measurements were performed in negative ion mode with a 25 µm x 25 µm field of view and a resolution of 200 nm/px. Using the integrated Gallium-FIB (30 kV, 1500 pA) the area was scanned 300 times resulting in a depth of around 1200 nm and an estimated layer thickness of around 4 nm. The intensity of the peaks associated with a particular element in the mass spectra is proportional to the number of ions of that species sputtered from the FIB sample interaction volume. It is important to note that the intensities do not provide compositional information since the yields of

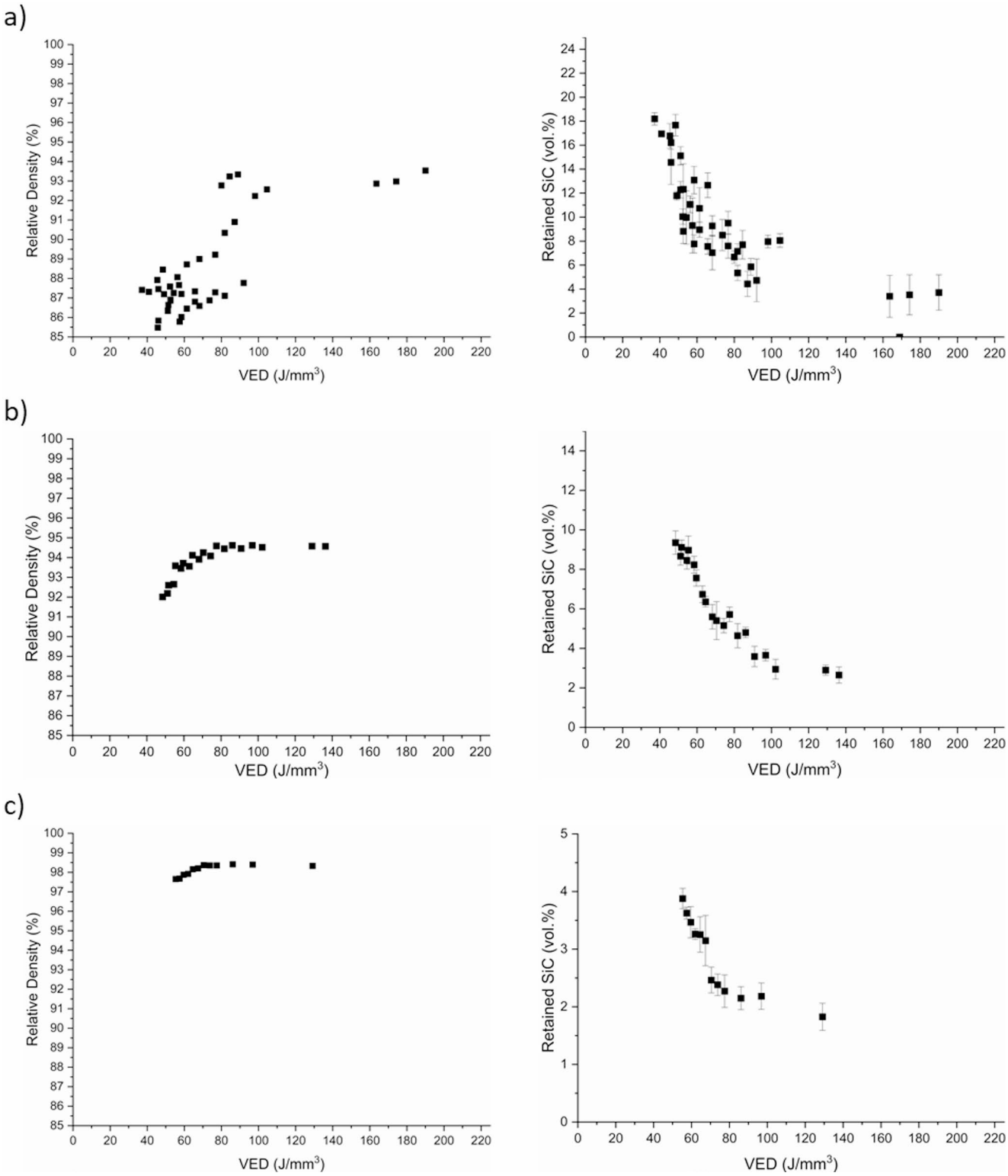

Fig. 5 Relative densities and retained SiC particles in correlation with the VED for (**a**) 25 vol% SiC, (**b**) 15 vol% SiC and (**c**) 5 vol% SiC starting compositions with error bars showing the standard deviation of all measurements

Table 5 Process parameters used for sample manufacturing

Starting Composition	*P* (W)	v (mm/s)	h (mm)	VED (J/mm^3)
25 vol% SiC	92	800	0.095	48
15 vol% SiC	92	700	0.095	55
5 vol% SiC	92	600	0.095	65

elemental secondary ions differ greatly across the periodic table. To create the 2D maps illustrated in Fig. 9, the total spectra for each specific location within the 2D map (pixel) were integrated sequentially across the 300 images (top view) and across the 125 horizontal pixels (front projection). While the top view provides similar data to the EDS mappings, the front projection provides further information showing that the oxygen concentration is highest in the

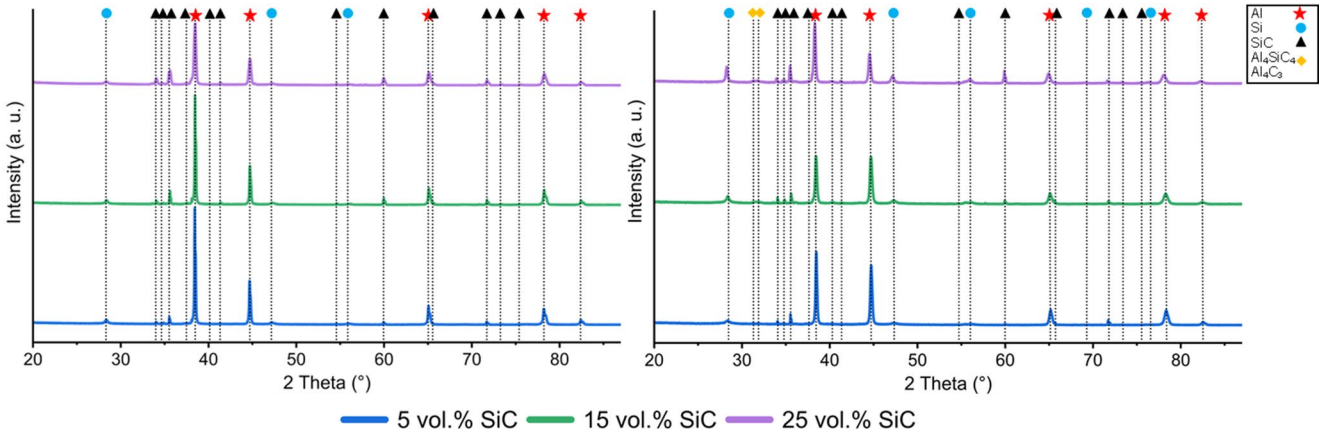

Fig. 6 XRD diffractograms from the starting powder compositions (left) and the LPBF manufactured samples (right)

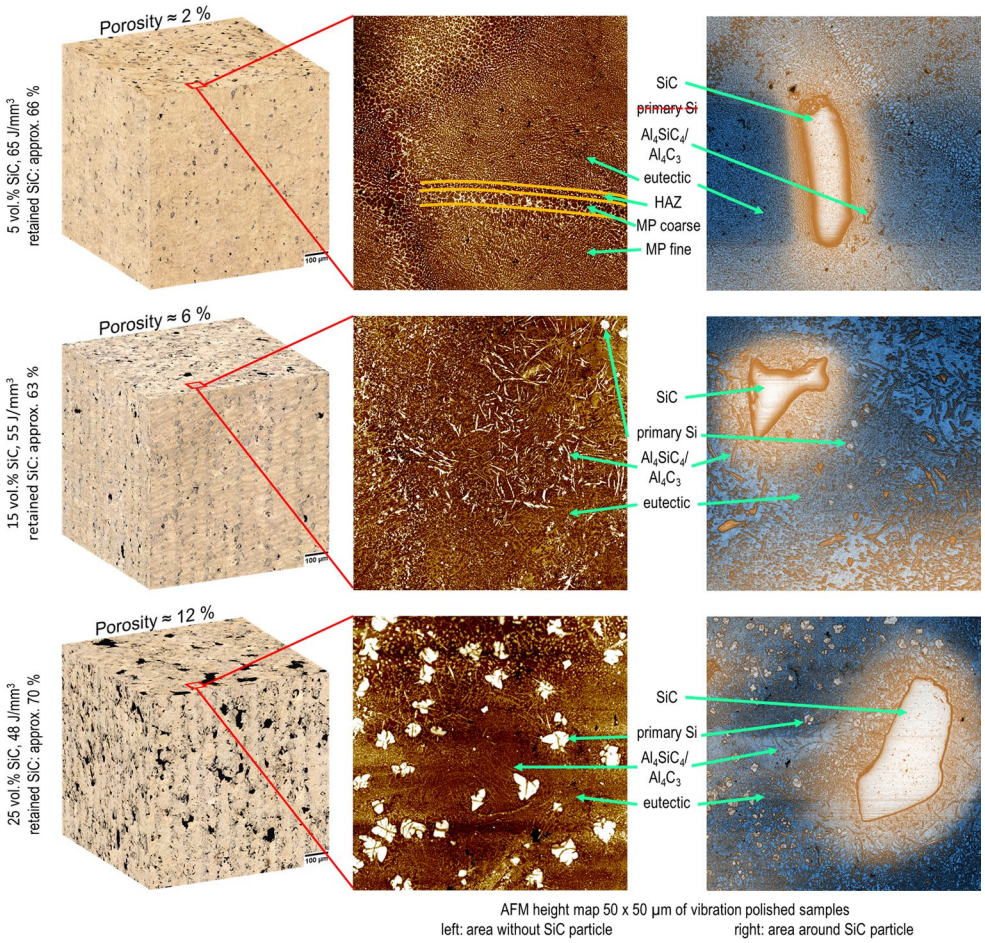

Fig. 7 Micrographs and AFM height maps (brighter = higher) for 5, 15 and 25 vol% SiC, respectively

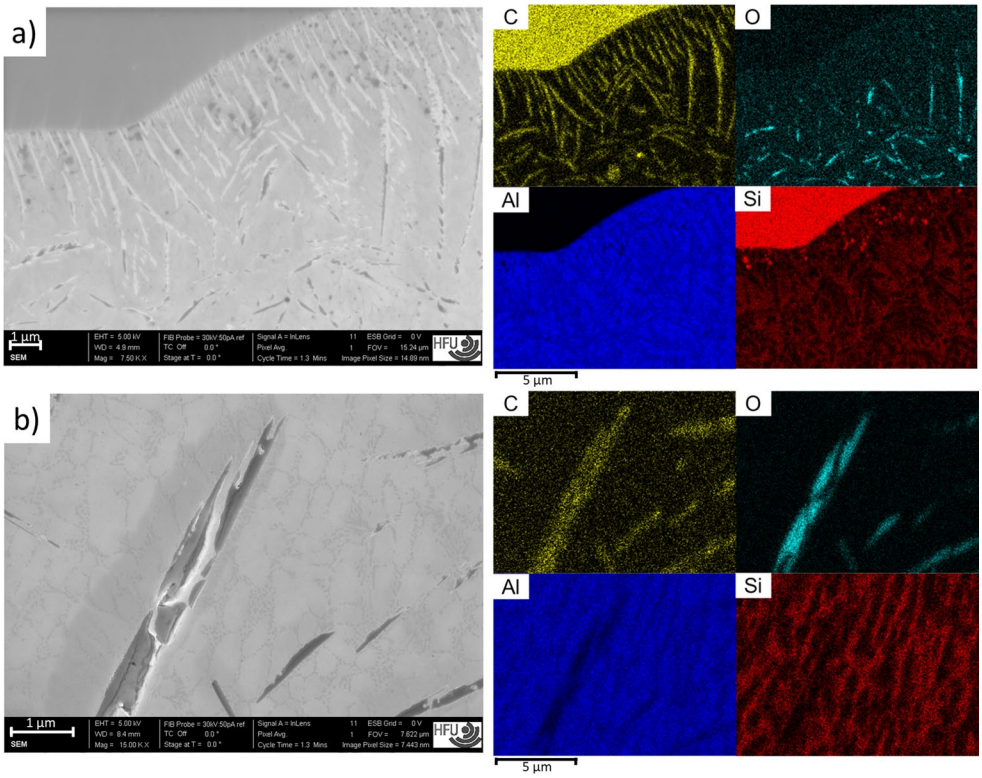

Fig. 8 SEM images and corresponding EDS mappings (**a**) at the SiC interface and (**b**) showing an oxygen rich region in detail

first layers. Additional depth profiles for oxygen and carbon are shown to illustrate the change in concentrations. While the carbon concentration (disregarding the first two layers) gradually increases in the first 100 layers (400 nm), the oxygen concentration shows an opposite trend in the same depth profile. In deeper layers, both concentrations reach a plateau.

4 Discussion

The presented results indicate a clear influence of process parameters and SiC content on the resulting material properties. When comparing low and high VEDs shown in Table 4 in combination with Fig. 3 it is evident, that high energy densities (> 100 J/mm^3) result in deformed surface planes of the manufactured samples. The severity of the deformation gets worse with increasing VED, especially when the hatch spacing decreases simultaneously which can even lead to failure of the build process as demonstrated by sample no. 13. It is proposed, that the deformation is mainly a result of evaporation and spattering of material caused by an overheated melt pool reaching the boiling point of aluminum and the bursting of SiC particles due to thermal shock. SiC particles can lead to an increase in absorbed energy since their absorptivity is high (78% [26]) in comparison to the aluminum alloy (25% [27]) resulting in a localized temperature surge [25, 28, 29]. When the hatch spacing is reduced, the focused laser spot hits more SiC particles and the effects described before are enhanced. This mechanism is supported by the microstructures observed in Fig. 4 showing drastically reduced volume fraction of SiC with increasing VED and smaller hatch spacing, consistent with the observations made by Astfalck et al. [21]. The resulting chessboard pattern can also be linked directly to this effect. Due to the chosen scanning strategy the laser systematically avoids certain areas where the intact SiC particles can be found. Further analysis of the laser interaction with SiC particles was conducted using pure SiC powder. It could be proven that SiC particles can melt incongruently at low VEDs, as shown in Fig. 10a), and burst due to the thermal shock [32], resulting in displaced powder particles in the immediate vicinity of the laser spot. It should be noted that more energy is probably required for the same effect in the powder mixture, as the aluminum powder respective the forming melt reduces the energy that the SiC particles are exposed to. This explains why some of the SiC particles remain intact even at much higher VEDs. The influence of the used VED on the retained SiC particles for all compositions are presented in Fig. 5 and agree with the results discussed before. Figure 5 additionally shows that the quantity of retained SiC particles correlates negatively with the achievable density for all compositions since lower VEDs lead to insufficient melting of the aluminum matrix. It is also evident that it is easier to obtain high densities when the volume fraction of SiC particles in the samples is lower, even at the same VEDs.

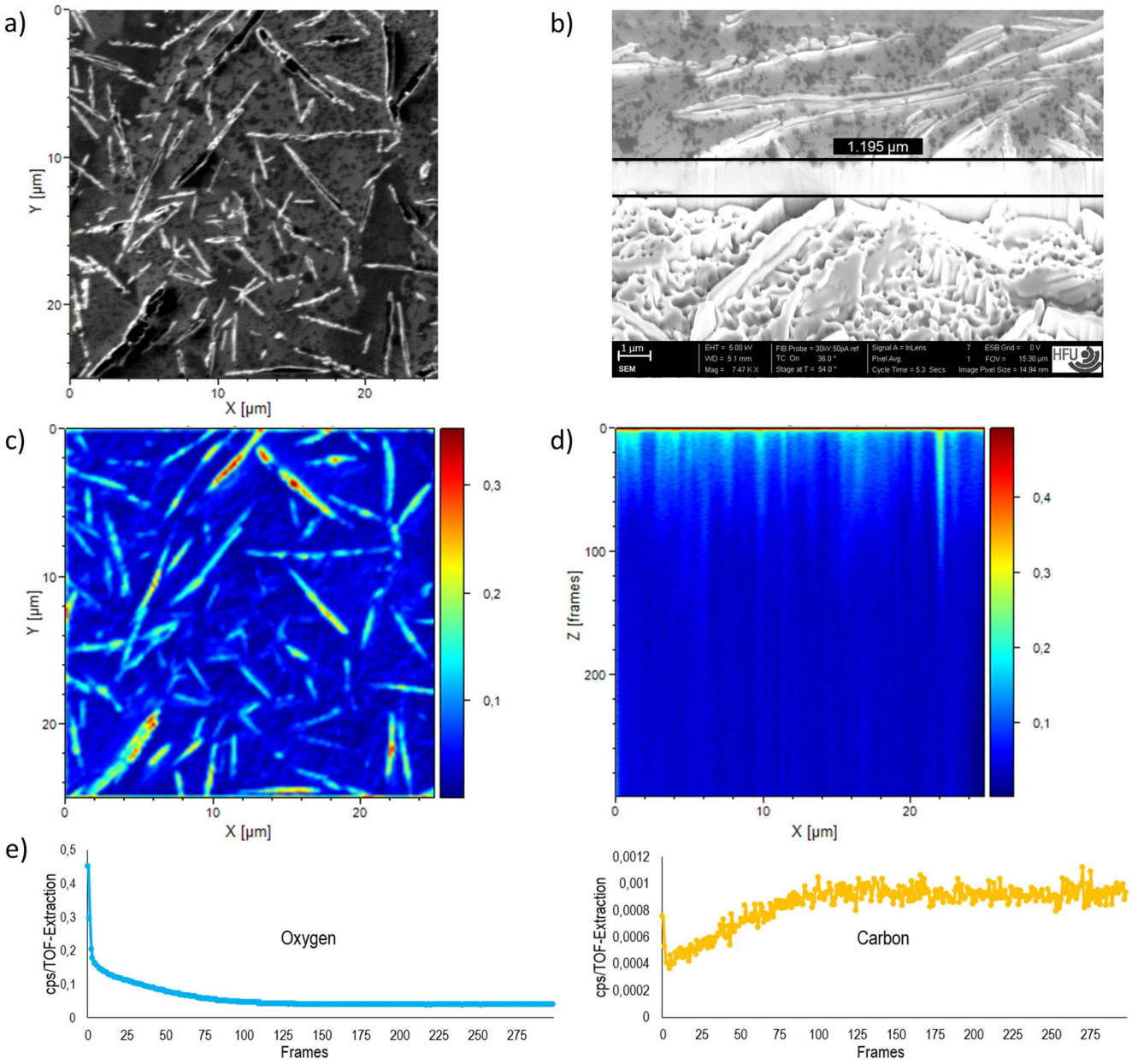

Fig. 9 Results of the TOF-SIMS analysis, showing (**a**) the analyzed field of view (25 µm x 25 µm) during the measurement, (**b**) the depth measurement after TOF-SIMS, (**c**) the top view of the oxygen concentration, (**d**) the front projection of the oxygen concentration, (**e**) depth profiles for the oxygen and carbon concentrations

This can be attributed to the pinning of the melt to the solid SiC particles which in consequence hinders the melt flow and can lead to interrupted melt tracks resulting in pores. Similar observations made by Zou et al. [33] and Chang et al. [23] support this conclusion. Additionally, when a larger fraction of SiC particles is added, the localized rise of the melt pool temperature due to higher energy absorption of SiC particles can also lead to more pronounced evaporation resulting in greater instabilities and increased defect formation [33–35]. All the mechanisms discussed before are illustrated in Fig. 10b).

Depending on the desired application, the results presented make it necessary to compromise between the required density and the retention of SiC particles. The described thermal degradation of SiC particles also changes the phase composition observed in the samples. The diffraction patterns illustrated in Fig. 6 show a substantial increase of the Si reflexes while the intensity of the SiC reflexes decreases and the additional phases Al_4C_3 and Al_4SiC_4 can be identified. These results can be explained with the observed microstructures (Fig. 7) in combination with the binary Al-Si phase diagram (Fig. 11a). When the

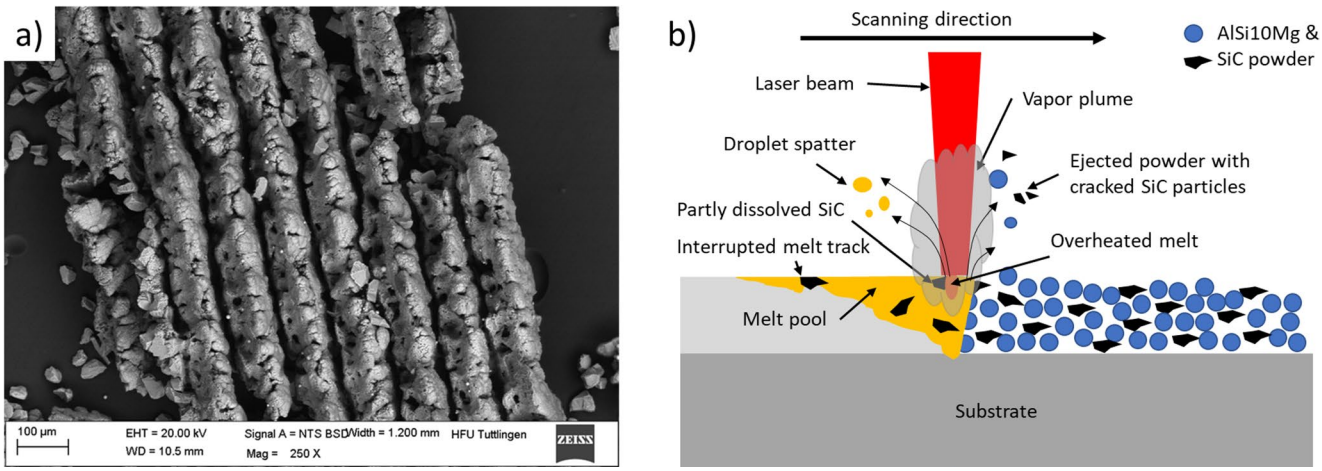

Fig. 10 Further analysis of LPBF process showing the (**a**) SEM image of pure SiC powder after being exposed to 46 J/mm^3, and (**b**) schematic illustration of the proposed mechanisms during LPBF of AlSi10Mg/SiC composite material

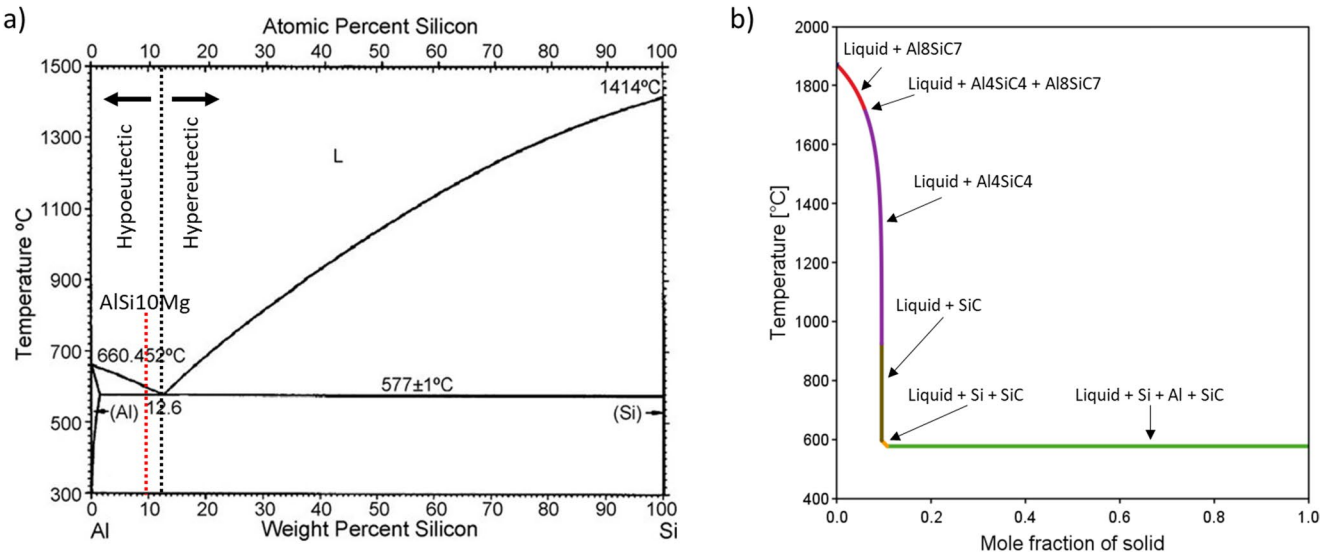

Fig. 11 Assessment of the microstructure after the LPBF process with help of the (**a**) Al-Si binary phase diagram [38], (**b**) calculated Scheil-Gulliver solidification simulation for the sample with 15 vol% SiC and a composition according to Table 6 using Thermo-Calc and the TCAL9 database

Table 6 Calculated compositions after the LPBF process, assuming a homogeneous mixture of AlSi10Mg and the degraded SiC

		Resulting composition wt%		
	Degraded SiC	Si	C	Al
AlSi10Mg	-	9.6	0	Balance
+5 vol% SiC	34%	10.8	0.6	Balance
+15 vol% SiC	37%	13.5	1.9	Balance
+25 vol% SiC	30%	14.8	2.6	Balance

temperature of SiC particles increases to 3100 K or above, a silicon melt with significant carbon content is formed [36, 37]. The high temperature in combination with the melt pool dynamics leads to quick mixing between the carbon rich silicon melt and the melt of the aluminum alloy. According to the calculated compositions shown in Table 6, if enough SiC particles get dissolved, the silicon content can increase enough to change the composition of the aluminum alloy from hypoeutectic to hypereutectic (Fig. 11a). The calculations assume a homogenous mixture of AlSi10Mg and the carbon rich silicon melt in the whole sample. Since this is an idealization, it is likely that there are local areas with higher and others with lower silicon and carbon content. This change results in the formation of primary Si crystals which could be observed in the samples with 15 vol% and 25 vol% SiC starting composition as shown in Fig. 7. An exemplary Scheil-Gulliver solidification simulation for the sample with 15 vol% SiC and the calculated composition from Table 6 is shown in Fig. 11b) and supports the suspected formation

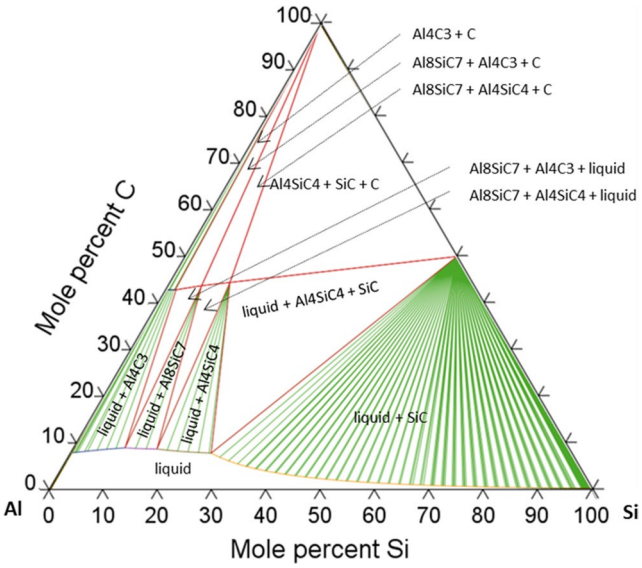

Fig. 12 Calculated isothermal section of the Al-Si-C system at 2000 °C using Thermo-Calc and the TCAL9 database

of primary silicon, even under idealized conditions. It is important to note that the Scheil-Gulliver solidification simulation does not account for the kinetics of phase formation. This is significant when the newly formed phases are discussed later on.

Besides this, the morphology of the eutectic structure can change. The effect of SiC particles seems negligible in samples with only 5 vol% SiC added, showing a typical eutectic structure for the AlSi10Mg alloy, consisting of a fine cellular network as previously described. With increasing SiC content and the resulting changes in composition and induced thermal energy, the morphology of the network changes. At 15 vol% SiC it starts to break up and shows more of a dendritic structure around SiC particles, where presumably the laser induced thermal energy is increased. For 25 vol% added SiC this effect is even greater, as can be seen in Fig. 7. In addition, three reactions with the carbon in the melt are thermodynamically possible forming the carbides Al_8SiC_7, Al_4SiC_4 and Al_4C_3, as shown in Fig. 12. Since the formation of Al_8SiC_7 is described in the literature as very slow and diffusion-limited [37, 39] it is very unlikely to form due to the extremely high cooling rates occurring during the LPBF process. In comparison Al_4SiC_4 formation is kinetically favored [39].

Al_4SiC_4 formation is reported among others by Gu et al. [22], Chang et al. [23], Xue et al. [29] and Zou et al. [33] for LPBF manufactured AlSi10Mg/SiC composites with different compositions. In contrast Astfalck et al. [21,] Famodimu et al. [24] and Xie et al. [40] report the formation of the Al_4C_3 phase, which is generally seen as unfavorable due to its instability in contact with water or moisture [41], where it can react according to reaction (4) [42] respective reaction (5) [43]:

$$Al_4C_3 + 12H_2O \rightarrow 4Al(OH)_3 + 3CH_4 \quad (4)$$

$$Al_4C_3 + 8H_2O \rightarrow 4AlOOH + 3CH_4 \quad (5)$$

In the thermodynamic equilibrium state, the Al_4C_3 phase should not form for the investigated compositions but its formation is reportedly strongly favored kinetically [39]. This makes its formation significantly more likely due to the short reaction times and consequential limited diffusion mechanisms during LPBF. As it is difficult to differentiate between Al_4SiC_4 and Al_4C_3 solely on the basis of the diffraction patterns shown in Fig. 6 due to the similarities, further analyses were carried out using SEM, EDS and TOF-SIMS on polished samples that had been exposed to ambient air for a prolonged period. EDS measurements (Fig. 8) showed two distinct areas. In direct vicinity to SiC particles areas with no increase in measured oxygen were observed, while other areas showed a significantly elevated oxygen level correlating with the observed plate-like phase which was previously identified as Al_4SiC_4 or Al_4C_3. Simultaneously carbon can be detected in both areas where the plate-like phase is visible. It is proposed, that Al_4SiC_4 can form near to SiC particles due to favorable compositions, short diffusion distances and elevated temperatures. However, the presence of oxygen in the other localized regions supports the theory that for kinetic reasons, Al_4C_3 is predominantly formed during the process, which leads to the formation of AlOOH after the reaction with moisture in the ambient air most likely according to reaction (5) [43]. The visible cracks in the oxygen rich area (Fig. 8b)) further support this assumption, as the formation of AlOOH as well as $Al(OH)_3$ leads to an increase in volume [43, 44]. Additionally, the TOF-SIMS measurements shown in Fig. 9 support the described mechanisms and allow the analysis of the depth of the hydroxide formation. It can be estimated that each layer of the TOF-SIMS measurement has a depth of 4 nm, since 300 layers were scanned and the total depth was approx. 1200 nm. High amounts of oxygen and carbon were detected in the first two layers, which can be attributed to the oxide layer formed on the aluminum alloy as well as to impurities from the preparation steps (e.g. cleansing with ethanol) or the environment. For the next 100 layers (400 nm) the depth profiles of detected carbon and oxygen ions follow opposite trends. While the measured oxygen intensity drops down, the carbon intensity increases until both reach a plateau. This behavior follows the expectations based on reaction (5). The surface layer of Al_4C_3 reacts with the moisture of the surrounding air to AlOOH and CH_4. As a

result, its volume increases, leading to localized cracks and freshly exposed surface areas which in consequence triggers further reactions that lead to the observed reduced carbon and increased oxygen concentration deeper in the material. The observed depth of the resulting hydroxide formation reached approx. 400 nm in the analyzed sample. It should be noted that the resulting defects can have a negative effect on the mechanical properties, even if the depth of the reaction is very low. Additionally, it is assumed that reaction (4) in liquid H_2O propagates much faster [43].

5 Conclusion

In this study AlSi10Mg/SiC metal matrix composites with different compositions were successfully manufactured using laser powder bed fusion and analyzed regarding density, microstructure and formed phases. The main conclusions could be drawn as follows:

1) The maximal reached relative density varied depending on the SiC fraction (lower SiC = higher density) and the used volumetric energy density (higher VED = higher density). For SiC fractions of 25 vol% ≈ 93.0%, 15 vol% ≈ 94.5% and 5 vol% ≈ 98.5% could be achieved.
2) Higher relative densities correlated with a strongly reduced fraction of retained SiC after the LPBF process. Due to the necessity for higher VED to achieve the higher densities, stronger thermal degradation of the SiC particles occurred. As a result, compromises between porosity of the samples and the resulting SiC content were necessary. Thermal degradation is proposed as the most possible theory, since it could be proven that SiC particles can be decomposed with relatively low energy density (≈40 J/mm^3) and strong materials loss due to evaporation was visible at high VED.
3) Thermal degradation of SiC particles was present in all tested samples, increasing with higher SiC content and higher energy density, resulting in plate-like Al_4C_3 and Al_4SiC_4 as well as increased Si content. Predominately Al_4C_3 formed in the samples due to kinetic reasons and the extremely quick solidification during LPBF. When higher SiC fractions (≥15 vol%) were present primary silicon crystals formed due to a shift of the silicon content in the melt from hypoeutectic to hypereutectic as calculations and an exemplary Scheil simulation demonstrated.
4) EDS and TOF-SIMS measurements confirmed the presence of oxygen after polished samples were left in ambient atmosphere for a prolonged period of time proving the presence of Al_4C_3 which reacted with the humidity of the air to AlOOH leading to localized cracks.
5) Excellent wetting of the SiC particles by the AlSi10Mg matrix was observed. Due to possible reactions between melt and SiC chemical bonding of the particles is possible. Despite the short reaction times and the high cooling rates during LPBF no micro-pores or -cracks were spotted at the interface.

While this study successfully demonstrated the manufacturability of AlSi10Mg/SiC composites using LPBF and characterized the resulting microstructure, several limitations were identified, which in turn open opportunities for future research. This study's main limitations include the inherent trade-off between achieving low porosity (which requires high VED) and preventing the thermal degradation of SiC particles. Furthermore, the rapid LPBF process kinetically favors the formation of unstable Al_4C_3, which reacts with humidity or H_2O to form AlOOH resulting in localized micro-cracks, posing a risk to structural integrity. Future investigations are needed to evaluate the long-term environmental stability and mechanical properties (like strength and fatigue life) of these composites. Additionally, EBSD analysis should be done to evaluate the influence of the SiC particles, as well as the change from hypoeutectic to hypereutectic, on the grain formation, orientation and distribution. Further research should also focus on process optimization, such as post-processing with HIP, or alternative laser sources.

Author contributions The conception and design of the study were undertaken by Hadi Mozaffari-Jovein and Achim Conzelmann. Material preparation, data collection and analysis were performed by Achim Conzelmann. The first draft of the manuscript was written by Achim Conzelmann with Hans Jürgen Seifert and Hadi Mozaffari-Jovein reviewing and editing previous versions of the manuscript. All authors read and approved the final manuscript.

Funding Open Access funding enabled and organized by Projekt DEAL. This research was supported by the "Central Innovation Programme for small and medium-sized enterprises (SMEs)" of the Federal Ministry for Economic Affairs and Climate Action. The FIB-SEM was funded by the Deutsche Forschungsgemeinschaft (DFG, German Research Foundation), within the program Major Research Instrumentation (Project number: 505067193) under GG91b and by the state Baden-Württemberg as well as by Furtwangen University.

Declarations

Conflict of interest The authors declare that they have no known competing financial interests or personal relationships that could have appeared to influence the work reported in this paper.

Open Access This article is licensed under a Creative Commons Attribution 4.0 International License, which permits use, sharing, adaptation, distribution and reproduction in any medium or format, as long as you give appropriate credit to the original author(s) and the source, provide a link to the Creative Commons licence, and indicate if changes were made. The images or other third party material in this

article are included in the article's Creative Commons licence, unless indicated otherwise in a credit line to the material. If material is not included in the article's Creative Commons licence and your intended use is not permitted by statutory regulation or exceeds the permitted use, you will need to obtain permission directly from the copyright holder. To view a copy of this licence, visit http://creativecommons.org/licenses/by/4.0/.

6 References

1. Attar H, Calin M, Zhang LC, Scudino S, Eckert J (2014) Manufacturing by selective laser melting and mechanical behavior of commercially pure titanium. Mater Sci Eng A 593:170–177. https://doi.org/10.1016/j.msea.2013.11.038
2. Röttger A, Boes J, Theisen W, Thiele M, Esen C, Edelmann A, Hellmann R (2020) Microstructure and mechanical properties of 316L austenitic stainless steel processed by different SLM devices. Int J Adv Manuf Technol 108:769–783. https://doi.org/10.1007/s00170-020-05371-1
3. Sélo RRJ, Catchpole-Smith S, Maskery I, Ashcroft I, Tuck C (2020) On the thermal conductivity of AlSi10Mg and lattice structures made by laser powder bed fusion. Addit Manuf 34:101214. https://doi.org/10.1016/j.addma.2020.101214
4. Conner BP, Manogharan GP, Martof AN, Rodomsky LM, Rodomsky CM, Jordan DC, Limperos JW (2014) Making sense of 3-D printing: creating a map of additive manufacturing products and services. Addit Manuf 1:64–76. https://doi.org/10.1016/j.addma.2014.08.005
5. Li XP, Wang XJ, Saunders M, Suvorova A, Zhang LC, Liu YJ, Fang MH, Huang ZH, Sercombe TB (2015) A selective laser melting and solution heat treatment refined Al–12Si alloy with a controllable ultrafine eutectic microstructure and 25% tensile ductility. Acta Mater 95:74–82. https://doi.org/10.1016/j.actamat.2015.05.017
6. Shipley H, McDonnell D, Culleton M, Coull R, Lupoi R, O'Donnell G, Trimble D (2018) Optimisation of process parameters to address fundamental challenges during selective laser melting of Ti-6Al-4V: a review. Int J Mach Tools Manuf 128:1–20. https://doi.org/10.1016/j.ijmachtools.2018.01.003
7. Sinha A, Swain B, Behera A, Mallick P, Samal SK, Vishwanatha HM, Behera A (2022) A review on the processing of aero-turbine blade using 3D print techniques. J Manuf Mater Process 6(1):16. https://doi.org/10.3390/jmmp6010016
8. Tyflopoulos E, Lien M, Steinert M (2021) Optimization of brake calipers using topology optimization for additive manufacturing. Appl Sci 11(4):1437. https://doi.org/10.3390/app11041437
9. Guo L, Naghavi SA, Wang Z, Varma SN, Han Z, Yao Z, Wang L, Wang L, Liu C (2022) On the design evolution of hip implants: a review. Mater Des 216:110552. https://doi.org/10.1016/j.matdes.2022.110552
10. Dion G, Yamomo G, Howard J, Teeter M, Willing R, Lanting B (2020) Revision total knee arthroplasty using a novel 3D printed titanium augment: a biomechanical cadaveric study. J Mech Behav Biomed Mater 110:103944. https://doi.org/10.1016/j.jmbbm.2020.103944
11. Miracle DB (2005) Metal matrix composites – from science to technological significance. Compos Sci Technol 65:2526–2540. https://doi.org/10.1016/j.compscitech.2005.05.027
12. Tian C, Li X, Zhang S, Guo G, Wang L, Rong Y (2018) Study on design and performance of metal-bonded diamond grinding wheels fabricated by selective laser melting (SLM). Mater Des 156:52–61. https://doi.org/10.1016/j.matdes.2018.06.029
13. Xue C, Yu JK (2014) Enhanced thermal transfer and bending strength of SiC/Al composite with controlled interfacial reaction. Mater Des 53:74–78. https://doi.org/10.1016/j.matdes.2013.06.056
14. Yashpal, Sumankant CS, Jawalkar AS, Verma NM, Suri (2017) Fabrication of aluminium metal matrix composites with particulate reinforcement: A review. Mater Today: Proc 4(2):2927–2936. https://doi.org/10.1016/j.matpr.2017.02.174
15. Kennedy AR, Wyatt SM (2001) Characterising particle–matrix interfacial bonding in particulate Al–TiC MMCs produced by different methods. Compos - A: Appl Sci Manuf 32:55–559. https://doi.org/10.1016/S1359-835X(00)00052-X
16. Bodunrin MO, Alaneme KK, Chown LH (2015) Aluminium matrix hybrid composites: a review of reinforcement philosophies; mechanical, corrosion and tribological characteristics. J Mater Res Technol 4(4):434–445. https://doi.org/10.1016/j.jmrt.2015.05.003
17. Fenghong C, Chang C, Zhenyu W, Muthuramalingam T, Anbuchezhiyan G (2019) Effects of silicon carbide and tungsten carbide in aluminium metal matrix composites. Silicon 11:2625–2632. https://doi.org/10.1007/s12633-018-0051-6
18. Behera MP, Dougherty T, Singamneni S (2019) Conventional and additive manufacturing with metal matrix composites: a perspective. Procedia Manuf 30:159–166. https://doi.org/10.1016/j.promfg.2019.02.023
19. Gyansah L, Tariq NH, Tang JR, Qiu X, Gao JZ, Wang JQ, Xiong TY (2018) Cold sprayed additive manufacturing of SiC/Al metal matrix composite: synthesis, microstructure, heat treatment and tensile properties. Mater Sci Forum 932:62–75. https://doi.org/10.4028/www.scientific.net/MSF.932.62
20. Tarasova T, Gvozdeva G, Ableyeva R (2019) Aluminium matrix composites produced by laser based additive manufacturing. Mater Today Proc 11(1):305–310. https://doi.org/10.1016/j.matpr.2018.12.149
21. Astfalck LC, Kelly GK, Li X, Sercombe TB (2017) On the breakdown of SiC during the selective laser melting of aluminum matrix composites. Adv Eng Mater 19(8):1600835. https://doi.org/10.1002/adem.201600835
22. Gu D, Chang F, Dai D (2015) Selective laser melting additive manufacturing of novel aluminum based composites with multiple reinforcing phases. J Manuf Sci Eng 137(2):021010. https://doi.org/10.1115/1.4028925
23. Chang F, Gu D, Dai D, Yuan P (2015) Selective laser melting of in-situ al4SiC4+SiC hybrid reinforced al matrix composites: influence of starting SiC particle size. Surf Coat Tech 272:15–24. https://doi.org/10.1016/j.surfcoat.2015.04.029
24. Famodimu OH, Stanford M, Oduoza CF, Zhang L (2018) Effect of process parameters on the density and porosity of laser melted AlSi10Mg/SiC metal matrix composite. Front Mech Eng 13:520–527. https://doi.org/10.1007/s11465-018-0521-y
25. Gu D, Yang Y, Xi L, Yang J, Xia M (2019) Laser absorption behavior of randomly packed powder-bed during selective laser melting of SiC and TiB<Subscript>2</Subscript> reinforced Al matrix composites. Opt Laser Technol 119:105600. https://doi.org/10.1016/j.optlastec.2019.105600
26. Tolochko NK, Khlopkov YV, Mozzharov SE, Ignatiev MB, Laoui T, Titov VI (2000) Absorptance of powder materials suitable for laser sintering. Rapid Prototyp J 6(3):155–160. https://doi.org/10.1108/13552540010337029
27. Liao H, Zhu H, Xue G, Zeng X (2019) Alumina loss mechanism of Al_2O_3-AlSi10Mg composites during selective laser melting. J Alloys Compd 785:286–295. https://doi.org/10.1016/j.jallcom.2019.01.116
28. Wang Z, Zhuo L, Yin E, Zhao Z (2021) Microstructure evolution and properties of nanoparticulate SiC modified AlSi10Mg alloys. Mater Sci Eng A 808:140864. https://doi.org/10.1016/j.msea.2021.140864

29. Xue G, Ke L, Liao H, Chen C, Zhu H (2020) Effect of SiC particle size on densification behavior and mechanical properties of SiCp/AlSi10Mg composites fabricated by laser powder bed fusion. J Alloys Compd 845:156260. https://doi.org/10.1016/j.jallcom.2020.156260
30. Zhao X, Gu D, Ma C, Xi L, Zhang H (2019) Microstructure characteristics and its formation mechanism of selective laser melting SiC reinforced Al-based composites. Vacuum 160:189–196. https://doi.org/10.1016/j.vacuum.2018.11.022
31. Xue G, Ke L, Zhu H, Liao H, Zhu J, Zeng X (2019) Influence of processing parameters on selective laser melted SiCp/AlSi10Mg composites: densification, microstructure and mechanical properties. Mater Sci Eng A 764:138155. https://doi.org/10.1016/j.msea.2019.138155
32. Fan Z, Zhang J, Wang Z, Shan C, Huang C, Wang F (2024) A state-of-the-art review of fracture toughness of silicon carbide: implications for high-precision laser dicing techniques. Processes 12(12):2696. https://doi.org/10.3390/pr12122696
33. Zou T, Mei S, Chen M, Zhu H (2023) Influence of SiC content on microstructure and mechanical properties of SiCp/AlSi7Mg composites fabricated by selective laser melting. J Mater Eng Perform 32:296–304. https://doi.org/10.1007/s11665-022-07079-7
34. Gong H, Rafi K, Gu H, Starr T, Stucker B (2014) Analysis of defect generation in Ti-6Al-4V parts made using powder bed fusion additive manufacturing processes. Addit Manuf 1:87–98. https://doi.org/10.1016/j.addma.2014.08.002
35. Yang KV, Rometsch P, Jarvis T, Rao J, Cao S, Davies C, Wu X (2018) Porosity formation mechanisms and fatigue response in Al-Si-Mg alloys made by selective laser melting. Mater Sci Eng A 712:166–174. https://doi.org/10.1016/j.msea.2017.11.078
36. Sokolov PS, Mukhanov VA, Chauveau T, Solozhenko VL (2012) On melting of silicon carbide under pressure. J Superhard Mater 34:339–341. https://doi.org/10.3103/S1063457612050097
37. Gröbner J, Lukas HL, Aldinger F (1996) Thermodynamic calculation of the ternary system Al-Si-C. Calphad 20(2):247–254. https://doi.org/10.1016/S0364-5916(96)00027-2
38. Murray JL, McAlister AJ (1984) The Al-Si (aluminum-silicon) system. Bull Alloy Phase Diagr 5:74–84. https://doi.org/10.1007/BF02868729
39. Viala JC, Fortier P, Bouix J (1990) Stable and metastable phase equilibria in the chemical interaction between aluminium and silicon carbide. J Mater Sci 25:1842–1850. https://doi.org/10.1007/BF01045395
40. Xie H, Zhang J, Li F, Yuan G, Zhu Q, Jia Q, Zhang H, Zhang S (2021) Selective laser melting of SiCp/Al composites: densification, microstructure, and mechanical and tribological properties. Ceram Int 47(21):30826–30837. https://doi.org/10.1016/j.ceramint.2021.07.263
41. Yamaguchi A, Zhang S (1995) Synthesis and some properties of Al4SiC4. J Ceram Soc Jpn 103:20–24. https://doi.org/10.2109/jcersj.103.20
42. Simensen CJ (1978) Gas-chromatographic analysis of carbides in aluminium and magnesium. Z Anal Chem 292:207–212. https://doi.org/10.1007/BF00491809
43. Nýblová D, Billik P, Noga J, Šimon E, Bystrický R, Čaplovičová M, Nosko M (2018) Degradation of Al4C3 due to atmospheric humidity. JOM 70:2378–2384. https://doi.org/10.1007/s11837-018-3053-3
44. Rodríguez-Reyes M, Pech-Canul MI, Rendón-Angeles JC, López-Cuevas J (2006) Limiting the development of Al4C3 to prevent degradation of Al/SiCp composites processed by pressureless infiltration. Compos Sci Technol 66(7–8):1056–1062. https://doi.org/10.1016/j.compscitech.2005.07.025

Publisher's note Springer Nature remains neutral with regard to jurisdictional claims in published maps and institutional affiliations.